Precipitation behaviors in Ti-2.3 Wt Pct Cu alloy during isothermal and two-step aging

Reference:
Akamine Hiroshi, Mitsuhara Masatoshi, Nishida Minoru, Samaeeaghmiyoni Vahid, Schryvers Dominique, Tsukamoto Genki, Kunieda Tomonori, Fujii Hideki.- Precipitation behaviors in Ti-2.3 Wt Pct Cu alloy during isothermal and two-step aging
Metallurgical and materials transactions: A: physical metallurgy and materials science - ISSN 1073-5623 - New york, Springer, 52(2021), p. 2760-2772
Full text (Publisher's DOI): https://doi.org/10.1007/S11661-021-06265-X
To cite this reference: https://hdl.handle.net/10067/1782220151162165141

Title:

Precipitation behaviors in Ti-2.3 wt.%Cu alloy during isothermal and two-step aging

Authors and affiliations:

Hiroshi Akamine[1,*], Masatoshi Mitsuhara[1], Minoru Nishida[1], Vahid Samaee[2], Dominique Schryvers[2], Genki Tsukamoto[3], Tomonori Kunieda[3], Hideki Fujii[4]

1 Department of Advanced Materials Science and Engineering, Faculty of Engineering Sciences, Kyushu University, 6-1 Kasuga-koen, Kasuga 816-8580, Japan

2 Electron Microscopy for Materials Science (EMAT), University of Antwerp, Groenenborgerlaan 171, B-2020 Antwerp, Belgium

3 Nippon Steel Corporation, 20-1 Shintomi Futtsu, Chiba, 293-8511, Japan

4 Toho Titanium Co., Ltd., 3-3-5 Chigasaki, Kanagawa 253-8510, Japan

***corresponding author**

Abstract

Time-evolution of precipitate morphology related to age hardening behavior in Ti-2.3 wt.% Cu alloys is investigated with electron microscopy. A two-step aging, where the aging temperature was switched from 673 K to 873 K at 100 hours point, revealed that the hardness was drastically drops after switching the aging temperature. In the microstructure, characteristic V-shaped clusters of precipitates were observed, which were rarely observed in isothermal aging. It is revealed by transition of habit planes from $\{1\text{-}101\}_\alpha$ to $\{1\text{-}103\}_\alpha$ corresponding to the metastable and the stable precipitates, respectively, that the stable C11b-type Ti_2Cu precipitates are formed near the junction point of the V-shaped clusters. The drop of the hardness can be explained by a synergistic effect of coarsening of the precipitates, decrease of the number density, and diffusion-assisted relaxation of the strain field around the precipitates.

1. Introduction

Titanium and titanium alloys have been developed as functional and structural materials in a wide variety of fields including aviation, power plants, chemical industries, etc. To further extend their utility to other fields such as motorcycle and automotive industries, extensive efforts have been made for achieving both high strengths and good formability. Although the strategy for materials design depends on the type of titanium alloys, *i.e.* α, β, or $\alpha+\beta$ alloys [1,2], in this study we focus on α-type alloys. In α-type titanium alloys, high strengths can be attained by adding a specific amount of aluminum and/or oxygen to pure titanium for solid solution strengthening, both of which are stabilizers for the hexagonal close-packed α phase [1]. However, it has been reported that the addition of aluminum suppresses twinning deformation and decreases formability at room temperature compared to a pure titanium [3]. In order to keep the high formability based on twinning deformation, alternative elements for solid solution strengthening have been studied [4]. A commercialized Ti-Cu alloy approximately contains 1.0 wt.% Cu (Super-TIX® 10CU) [5] for solid solution strengthening. Because the solubility limit of copper in titanium is approximately 2.1 wt.% at the eutectoid point [6], precipitation of intermetallic Ti_2Cu compounds is suppressed in this alloy. Our interest here is a potential to utilize Ti_2Cu precipitates for further flexible materials design in Ti-Cu alloys with collaboration of solid-solution strengthening and precipitation strengthening. For this purpose, it is vital to understand precipitation behaviors in Ti-Cu alloys. In our previous study for Ti-2.3 wt.% Cu [7], we have found that the morphology of precipitates transforms from metastable fine precipitates to stable Ti_2Cu. The metastable fine precipitates are characterized by the habit planes parallel to pyramidal planes $\{1\text{-}101\}_\alpha$ of the hcp α matrix, whereas the stable Ti_2Cu has its habit planes parallel to $\{1\text{-}103\}_\alpha$ rather than pyramidal planes. For simplicity, here we denote metastable and stable precipitates as θ' and θ, respectively, as an analogy with Al-Cu alloys [8]. Importantly, it has been reported that the hardness is larger in the condition with fine θ' precipitates than with θ, which suggests that the transformation from θ' to θ phase is related to the hardness change. It is thus important to understand the precipitation process from supersaturated solid solution to equilibrium θ phase with aging treatments. In the present work, we study transformations from θ' to θ through microstructure observations for Ti-2.3 wt.% Cu alloys with different aging conditions.

2. Experimental

The chemical composition of the Ti-Cu alloy used in this study and prepared from the same ingot as inn the previous study [7], is shown in Table 1. The samples cut out from the hot-rolled sheets are fabricated to the size of $2 \times 2 \times 1$ mm^3. Each sample was sealed in a quartz tube in vacuum (approx. 2.7×10^{-4} Pa) and subjected to solution treatment and aging in a small-scale tube furnace. For solution treatment, samples were kept at 1063 K for 1 hour and subsequently quenched into ice water, where the quartz tube was broken to obtain high cooling rate. This temperature was selected so that the solid solubility of Cu in the α phase is maximized (approx. 2.1 wt.%) [6]. Isothermal aging was performed at 723 K to complement the previous agings at 673, 773, and 873 K [7] for a maximum duration of 1000 h. To observe the transition from θ' to θ, two-step aging was additionally performed, where the aging temperature was switched from 673 to 873 K. In switching, the vacuum-sealed quartz tube was quickly transferred from one furnace to the other, which took a few seconds. After aging for different periods, the samples were rapidly quenched into ice water. After the heat treatments, the samples were then polished with waterproof SiC sandpapers. The hardness was measured by using micro Vickers hardness testing equipment (Shimadzu, HMV-G).

The microstructures were examined by transmission electron microscopy (TEM), scanning TEM (STEM), and scanning electron microscopy (SEM). The specimens for TEM/STEM were prepared by electropolishing (Fischione Instruments, Model 140) with a mixture of perchloric acid and methanol ($HClO_4/CH_3OH$ = 6:94, vol. %) at around 253 K under a voltage of 20 V. TEM/STEM observations were made with Thermo Fischer Titan^3 G2 (Kyushu University) and Thermo Fischer QU-Ant-EM (EMAT, Antwerp University), both of which are equipped with a spherical aberration corrector on the probe-forming lenses and were operated at the acceleration voltage of 300 kV. SEM observations were performed with Carl Zeiss ULTRA55 (Kyushu University). Crystal orientation measurements and trace analyses of precipitates were performed by using electron backscattered diffraction (EBSD).

Table 1. Chemical composition (wt. %) of the alloy used in the present study.

C	**Ni**	**Cr**	**Cu**	**Fe**	**H**	**O**	**N**	**Ti**
0.003	0.011	0.001	2.26	0.020	0.001	0.034	0.005	Bal.

3. Results

3.1. Transformation in isothermal aging

Figure 1 shows an age hardening curve during isothermal aging at different temperature. The plots for 673 K, 773K, and 873 K are reproduced from the previous report [7]. In the previous measurements, the trend of the hardness change was clearly different between aging at 673 K and above 773 K. We have reported that the microstructure for each range of temperature is characterized by metastable precipitates (θ' phase) and stable Ti_2Cu precipitates (θ phase), respectively [7]. Importantly, concurrent precipitation of the θ' and the θ precipitates has been observed for aging at

873 K for 10 h, while only the θ precipitates are present in the later stage of aging at 873 K. In the age-hardening curve for the new intermediate temperature, 723 K, which is additionally measured in the present study, the hardness is continuously increased up to 600 h and slightly decreased in the later stage.

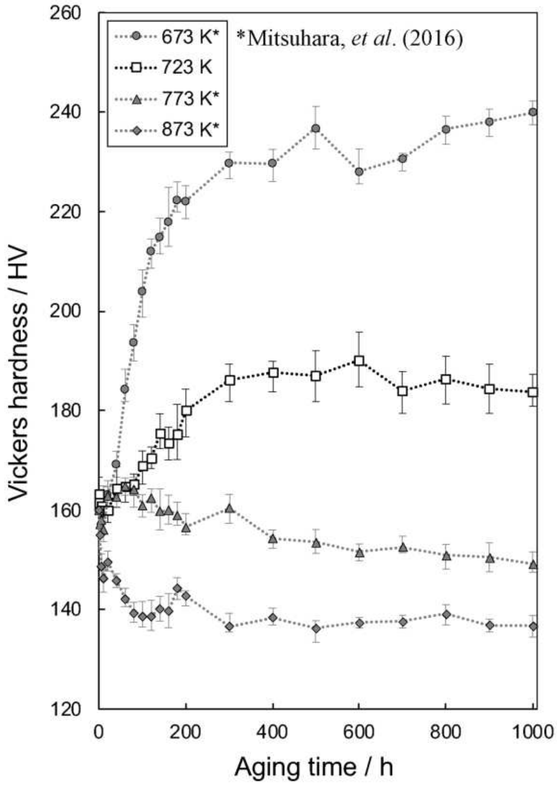

Fig. 1 Age-hardening curves under different aging temperatures. The curves for 673, 773, and 873 K are reproduced from Ref. [7].

To understand the transformation behavior in the age-hardening curve for the aging at 723 K, we studied which precipitates, θ' or θ, are dominant in the age-hardening behavior. Figures 2(a)-(c) show EBSD crystal orientation maps for 100, 600, and 1000 h at 723 K, and in which crystal directions parallel to the observation direction are colored according to the color key of the standard stereographic triangle attached in Fig. 2(c). Figs. 2(d)-(f) are SEM images obtained from the boxes in Figs. 2(a)-(c), respectively. Two types of precipitates can be distinguished by comparing traces of habit planes corresponding to the θ' and the θ precipitates, respectively [7]. The measured trace lines were categorized to $\{1\text{-}101\}_\alpha$ and $\{1\text{-}103\}_\alpha$ habit plane families based on the ideal trace lines calculated from the crystal orientations as shown in Figs. 2(g)-(i), where red and blue lines represent $\{1\text{-}101\}_\alpha$ and $\{1\text{-}103\}_\alpha$ planes, respectively. Note that the measured trace lines with large deviation from the ideal lines may be regarded as errors originated from surface roughness and/or resolution limit in the SEM images: these were removed from the counting. In the case that the calculated trace lines of two types of habit planes are close to each other, it becomes difficult to resolve the category. In the current analysis, such lines were also removed from the counting. The histograms of categorized precipitates were obtained as shown in Fig. 3. After aging at 723 K for 100 h, the θ' precipitates are mainly observed, whereas both of the θ' and the θ precipitates are present in the specimens aged at 723 K for 600 and 1000 h (Figs. 3(b) and 3(c)). The θ' precipitates are homogeneously distributed in the matrix at any stage, and the length distribution of the θ' precipitates is broadened with aging time, reaching about 2 μm long after the aging for 600 h. In contrast, the distribution of the θ precipitates is inhomogeneous, *i.e.*, often localized as denoted by white dashed boxes in Fig. 2(e) and 2(f), and the length is small even after long aging for 1000 h (Fig. 3(c)). The fraction of the θ precipitates is increased from 100 to 600 h aging, while remaining almost unchanged from 600 to 1000 h aging. This indicates that the transformation rates of both the θ' and the θ precipitates are significantly slowing down in the later stage of aging at 723 K.

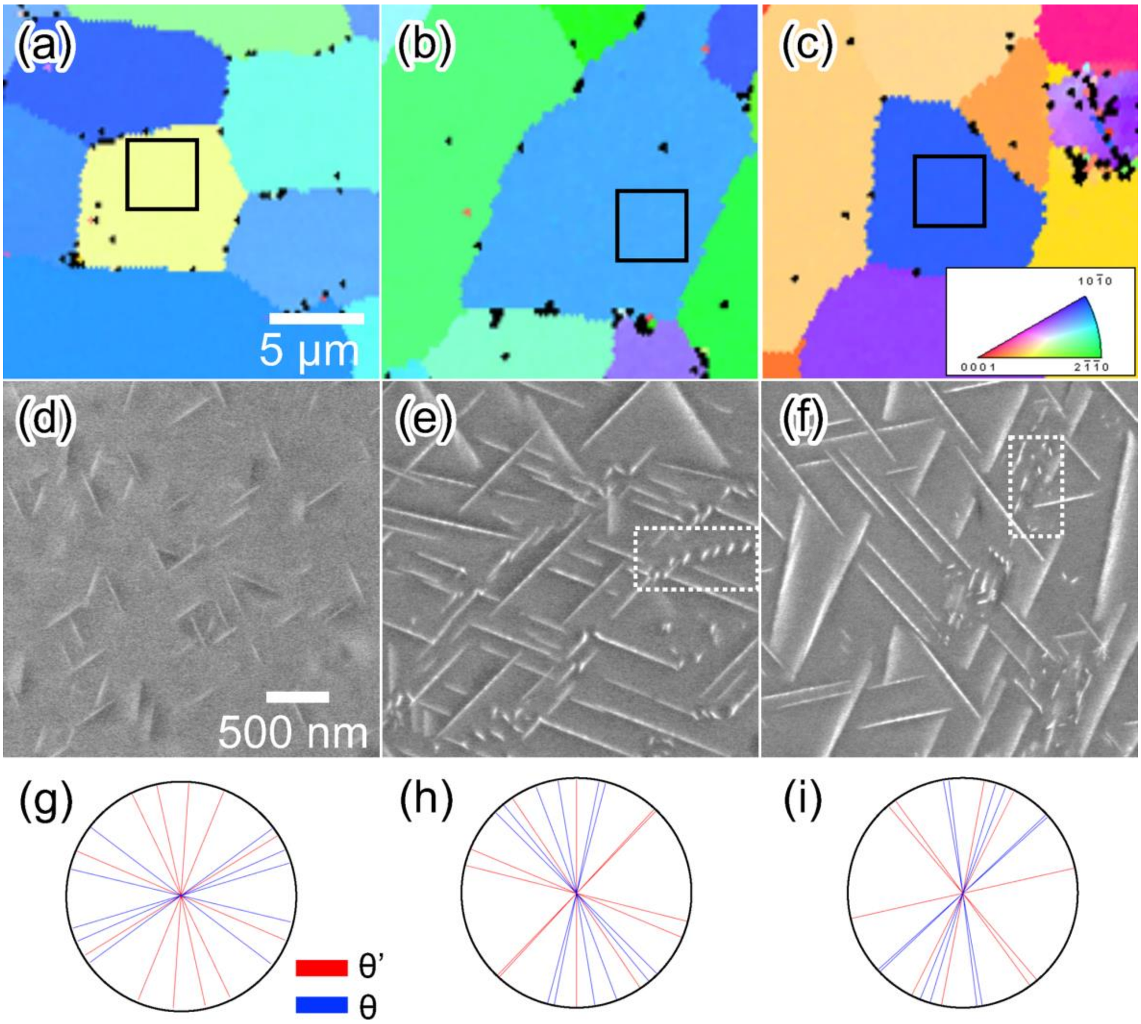

Fig. 2 (a)-(c) Crystal orientation maps for the specimen aged at 723 K for 100, 600, 1000 h, respectively. (d)-(f) SEM images obtained from the boxes in (a)-(c), respectively, and (g)-(i) corresponding trace lines calculated from the measured crystal orientations.

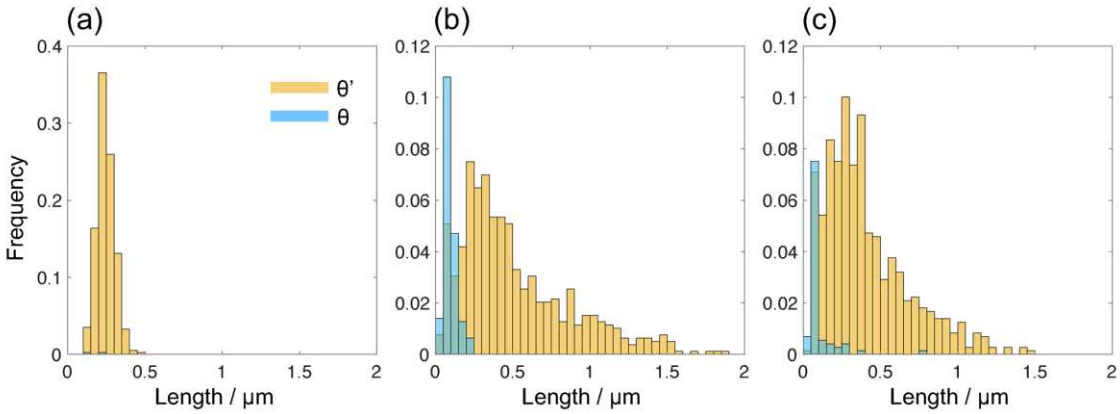

Fig. 3 Length histograms of θ' (orange) and θ (blue) precipitates for the specimen aged at 723 K for (a) 100 h, (b) 600 h, and (c) 1000 h, respectively. Frequency is normalized such that integration over two histograms (θ'+θ) yields unity.

To obtain further insights on the phase transformation between the θ' and the θ phases, a time-temperature-precipitate (TTP) diagram was constructed based on a number of TEM and SEM observations as shown in Fig. 4, from which the precipitates were distinguished by their habit planes. For aging at 673 K, TEM images were used for evaluation, and SEM images for 723 K or above. It appears that there is a region at 673 K and 723 K, where only the θ' precipitates are observed, and in the higher temperature region, the presence of both θ' and θ precipitates is more preferable. Comparing Fig. 4 to the age-hardening curve in Fig. 1, the single-phase region of the θ' precipitates at 673 K shows high hardness, whereas the two-phase region corresponds to lower hardness. This suggests that the precipitation of the θ phase is related to the age-hardening behaviors.

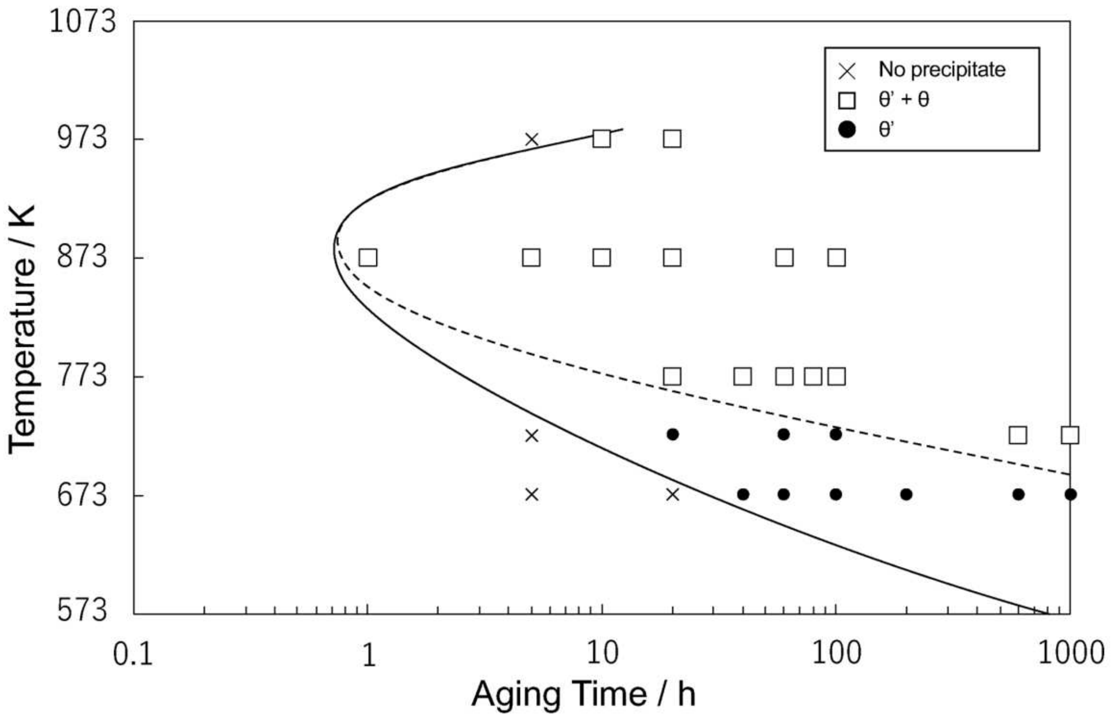

Fig. 4 Time-Temperature-Precipitate diagram for the Ti-2.3 wt.% Cu alloy constructed based on STEM and SEM observations. Open square indicates two phase regions of θ‘ and θ, filled circles single phase region of θ’, and cross marks means that no precipitates were observed.

3.2. Transformation in the two-step aging

In the next step, to reveal the behavior of the phase transformation via the phase boundary in the TTP diagram (Fig. 4), a two-step aging was performed. The first aging was done at 673 K for 100 h to introduce homogeneously distributed θ’ precipitates, and the second aging was performed at 873 K for 1, 10, and 100 h. The age-hardening curve of the specimen after the two-step aging is plotted in Fig. 5 together with the curves for the single step aging (Fig. 1) as shown in Fig. 5. It is notable that the curve for the two-step aging shows a large drop after switching the aging temperature and approaches to the curve for the single step aging at 873 K.

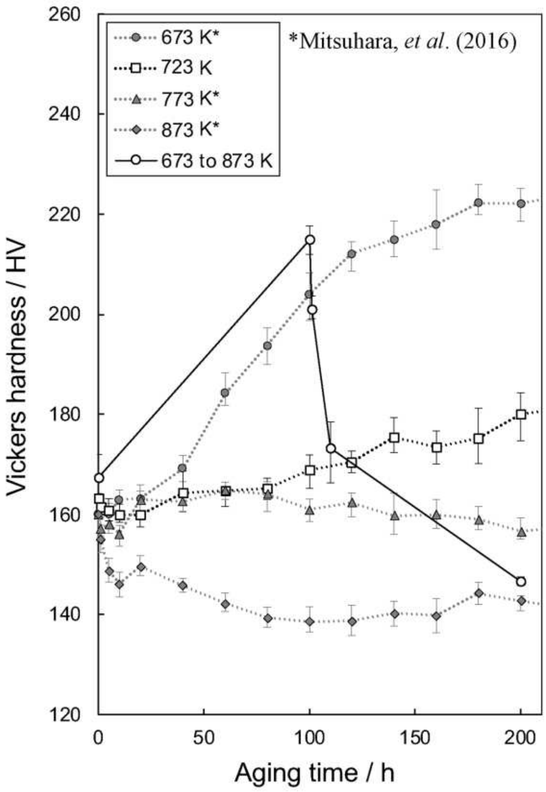

Fig. 5 Age-hardening curves for the two-step aging from 673 K for 100 h to 873 K for 100 h. For comparison, single-step aging curves for 673, 723, 773, and 873 K for this time-spun are plotted again.

Figures 6(a) and (b) show HAADF-STEM images of the specimen after the first step of aging. All of the HAADF-STEM images were observed along the $[11\text{-}20]_\alpha$ zone axis. As previously reported, only fine θ' precipitates are observed and the habit planes are parallel to $\{1\text{-}101\}_\alpha$ pyramidal planes [7,9]. In the high-magnification image (Fig. 6(b)), a periodic intensity similar to the arrangement of the θ precipitate is observed, but with a weak ordering of atoms as previously reported [7], where the amplitude of the intensity fluctuation is still small compared to the highly ordered θ precipitates (see Fig. 7). Figures 6(c) and (d) are HAADF-STEM images of the specimen after the second aging at 873 K for 1 h. Notably, two or three θ' precipitates are connected to each other and the habit planes are curved near the junctions. It is revealed that the habit planes near the junction are parallel to $\{1\text{-}103\}_\alpha$ planes that have been observed for isolated θ precipitates [7], and the junction plane forms a twin interface. The Miller index of the junction plane corresponds to $\{013\}_{C11b}$ of the θ phase, which are parallel to $\{0001\}_\alpha$ basal planes. It should be noted that the $\{1\text{-}101\}_\alpha$ habit planes are flat, while a part of the $\{1\text{-}103\}_\alpha$ habit planes includes periodic steps. This may suggest that the $\{1\text{-}101\}_\alpha$ planes are still stable in terms of the interfacial energy, whereas $\{1\text{-}103\}_\alpha$ habit planes are preferable when incorporating relaxation of macroscopic transformation strain.

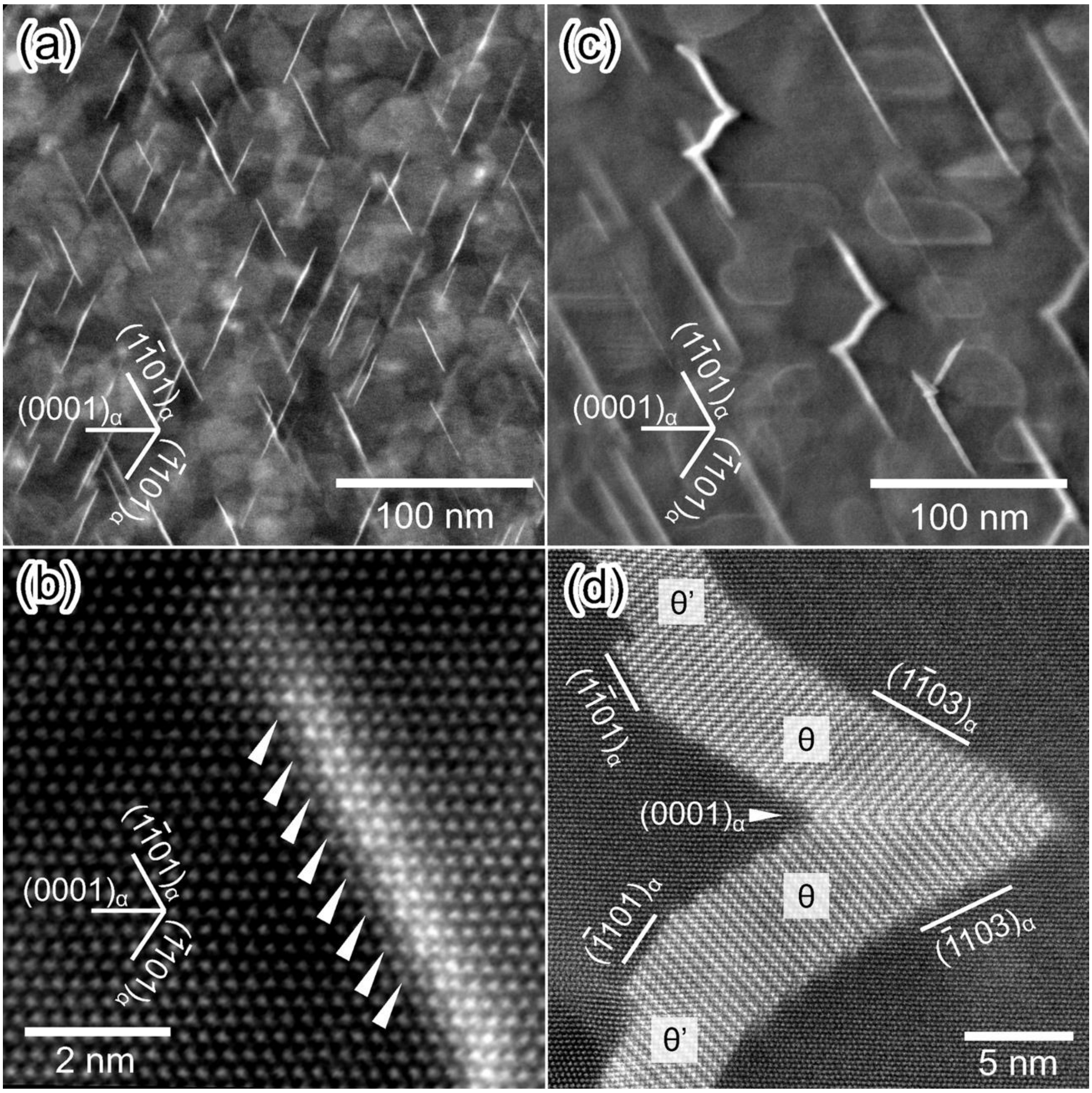

Fig. 6 STEM-HAADF images for the specimens (a), (b) aged at 673 K for 100 h and (c), (d) after the second aging at 873 K for 1 h.

Figures 7(a) and (b) show HAADF-STEM images of the specimen aged at 673 K for 100 h followed by the second aging at 873 K for 10 h. In the microstructure, many of the V-shaped precipitates are observed and the habit planes are composed of both $\{1\text{-}101\}_\alpha$ and $\{1\text{-}103\}_\alpha$, while the fraction of $\{1\text{-}103\}_\alpha$ has apparently increased from Fig. 6(c). Figure 7(b) shows an enlarged HAADF-STEM image of a V-shaped precipitate which has only $\{1\text{-}103\}_\alpha$ habit planes. The periodic intensity corresponding to the C11b-type ordered structure of the θ phase is clearly observed as well as in Fig. 6(d). A portion of precipitates is disc-shaped and has no twin interface or junction. Figures

7(c) and (d) show HAADF-STEM images for the specimen aged at 673 K for 100 h followed by the second aging at 873 K for 100 h. The size of the precipitates becomes larger and the number density of precipitates decreases. It appears that many of the precipitates are disc-shaped and the habit planes are mainly $\{1\text{-}103\}_{\alpha}$, indicating that the V-shaped cluster gradually transforms into an isolated disc-shaped precipitates and the θ phase becomes dominant.

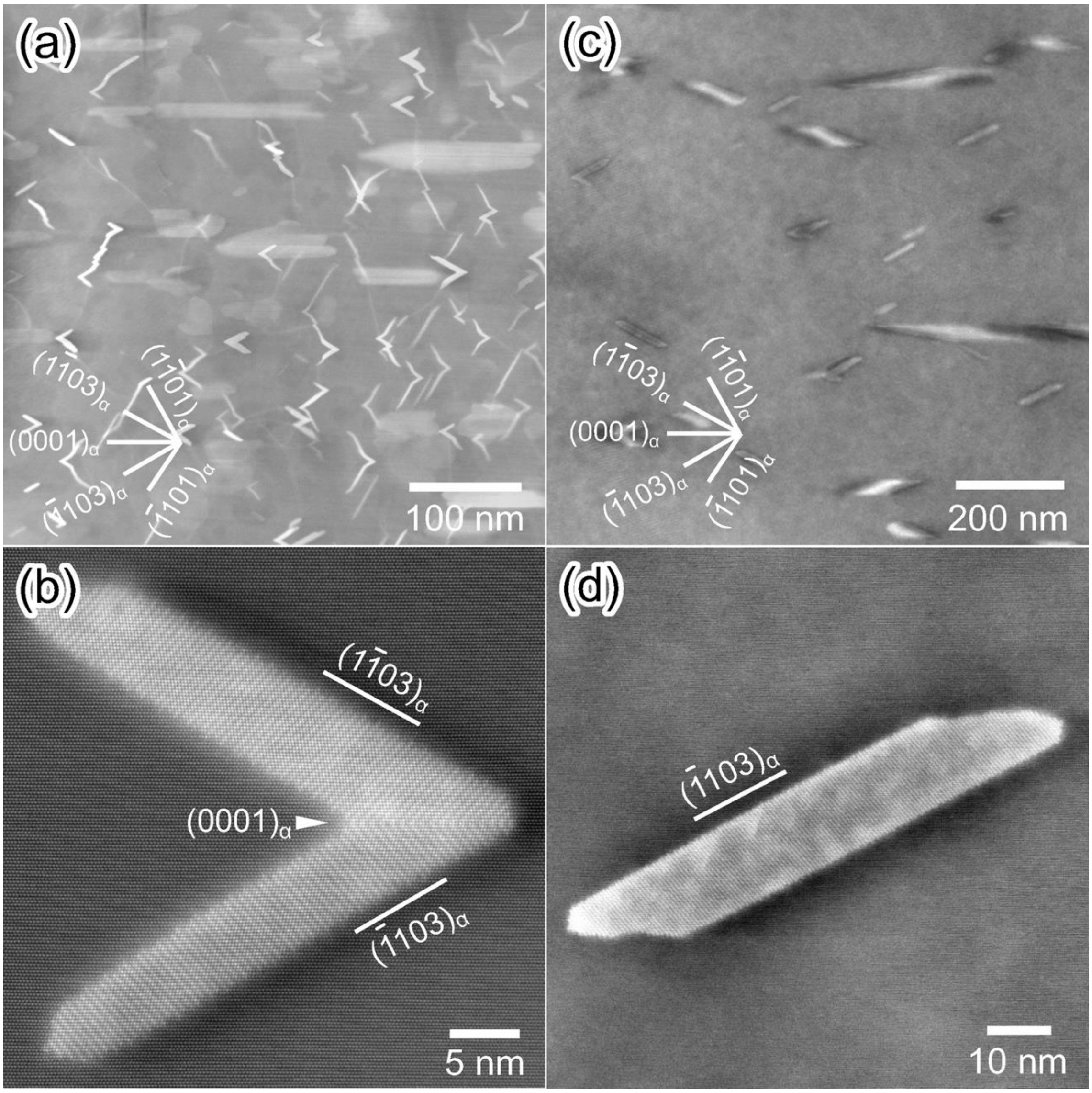

Fig. 7 STEM-HAADF images for the specimens after the second aging at 873 K for (a), (b) 10 h, and (c), (d) 100 h.

Figure 8(a) shows the time-development of the fraction of the θ phase in large precipitate regions. The fraction was estimated by measuring the length of precipitates with $\{1\text{-}103\}_{\alpha}$ habit planes in HAADF-STEM images. When a precipitate has a combined shape of both $\{1\text{-}101\}_{\alpha}$ and

$\{1\text{-}103\}_\alpha$ habit planes, the partial length of the $\{1\text{-}103\}_\alpha$ habit planes was measured. For instance, the parts *a* and *b* of the illustration in Fig. 8(a) are added up for the lengths of the θ' and the θ phases, respectively, and the fraction of the θ phase is calculated by dividing the total sum of the part *b* by the total sum of *a*+*b*. The zero point in the second aging time represents the state after the aging at 673 K for 100 h, *i.e.*, fine θ' precipitates are homogeneously distributed as shown in Fig. 6(b). It appears that the drastic increase of the θ phase is observed over the second aging time from 1 to 10 h, while it is not significantly changed between 10 to 100 h. Next, Fig. 8(b) shows the change in the number density of the precipitates with respect to the second aging time, counted in the HAADF-STEM images. Connected precipitates as shown in Fig. 6(d) and Fig. 7(b) are counted as a single precipitate, and the number density was calculated as the number per unit area in the field of view. Note that the thickness variation between the TEM specimens was not incorporated, because the field of view for each specimen was selected so that the thickness is comparable between the specimens and the influence of thickness variation is minimized compared to the dimension of the precipitates. The result in Fig. 8(b) indicates that the number density is largely dropped at the initial stage of the second aging for 1 to 10 h, while the decreasing rate is slowed down in the later stage. As observed in Fig. 6(c), this decrease may be related to coarsening and coalescence of the precipitates. It is expected that these microstructure changes contribute to the drop of the hardness in Fig. 5 at the initial stage of the second aging. However, it should be noted that the fraction of the θ phase for the second aging time of 1 h is only ~0.1, which is unexpectedly low compared to the large drop of the hardness in Fig. 5. This implies that the θ'-θ phase transformation itself is not enough to explain the drastic decrease in the hardness. To reveal another impact of the phase transformation underlying the drastic behavior of the age-hardening, further discussion will be provided below.

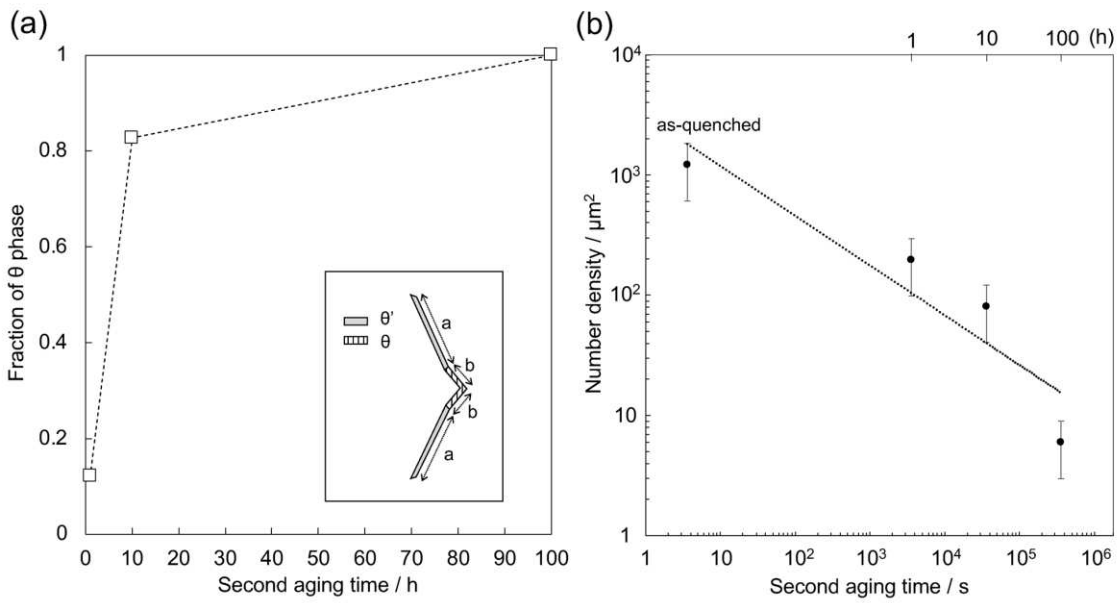

Fig. 8 (a) Development of fraction of θ phase in the regions occupied by precipitates during the second aging at 873 K. For the clustered precipitates including both phases, length of θ phase was measured as partial length of $\{1\text{-}103\}_{\alpha}$ habit planes denoted as b in the inset illustration in (a). (b) Development of the number density of the precipitates, in which clustered precipitates were counted as a single precipitate.

4. Discussion

Different precipitation behaviors of the θ' and the θ precipitates have been observed for isothermal and two-step aging. In the isothermal aging, the θ' and the θ precipitates are observed separately, and the size of θ' is larger than θ as shown in Fig. 2. This indicates that θ' and θ precipitates during the isothermal aging have independently nucleated. In contrast, many of the θ precipitates have continuously developed from the θ' precipitates during the two-step aging as shown in Figs. 6(c) and 6(d).

In the continuous development, multiple θ' precipitates are connected to each other and form a V-shaped clusters, which have a twin interface at the junction point, corresponding to $\{013\}_{C11b}$ parallel to the $\{0001\}_{\alpha}$ basal plane. After the second aging at 873 K for 1 h (Figs. 6(c) and 6(d)), the habit plane near the junction between two θ' precipitates is changed from $\{1\text{-}101\}_{\alpha}$ to $\{1\text{-}103\}_{\alpha}$ planes. In the later stage, $\{1\text{-}101\}_{\alpha}$ habit planes are gradually replaced by $\{1\text{-}103\}_{\alpha}$ habit planes during the second aging (Figs. 6(a) and 6(b)).

Importantly, many of the V-shaped clusters were observed during the second aging at 873 K, but rarely observed for the isothermal aging at 723 K as shown in Fig. 2. In the latter case, the θ' precipitates are simply elongated and touching with each other on a T-shaped junction, which is a more expected form of a junction between two θ' precipitates. One of the important differences between these aging conditions is diffusivity. The impurity diffusion coefficient of copper in α-titanium can be estimated from the previously reported linear Arrhenius plot [10] as 3.1×10^{-19} m^2s^{-1} at 723 K and 8.2×10^{-17} m^2s^{-1} at 873 K, respectively. Since the diffusion rate is proportional to the diffusion coefficient [11], the diffusion rate is nearly faster by nearly two orders of magnitude at 873 K compared to at 723 K. Alternatively, different aging conditions can be compared by the tempering parameter P [12], which is given by

$$P = T(\log t + A),$$

where T is absolute temperature, and t is the aging time in the unit of hours. A is a constant parameter typically set as A = 20 [12], and this study also follows this convention. The calculated tempering parameters are summarized in Table 2. It appears that the tempering parameter for aging at 723 K for 1000 h is even smaller than that at 873 K for 1 h. This indicates that the rate of microstructural evolution at 723 K is a lot slower than at 873 K. It is thus possible that the absence of V-shaped clusters for aging at 723 K is related to a too low aging time.

Table 2 Tempering parameters, *P*, calculated for aging at 723 K and 873 K.

Temperature (K)	**Aging time (h)**	**Tempering parameters**
723	1	14,460
723	10	15,183
723	100	15,906
723	1000	16,629
873	1	17,460
873	10	18,333
873	100	19,206

Figure 9(a) is a picture of a premature state of a cluster observed on the specimen after the second aging at 873 K for 1 h, where two θ’ precipitates are about to connect. Interestingly, the contrast of the HAADF-STEM image is diffused near the junction, implying that the θ’ precipitates are disordered and/or resolved into the matrix. Figure 9(b) is a HAADF-STEM image of a V-shaped cluster that is more developed than in Fig. 9(a). It should be noted that an anti-phase boundaries (APBs) can be found at the interface between the θ’ and the θ regions for which we ignore the small rotation between the θ’ and the θ regions and suppose that the crystal structures of the θ’ and the θ are the same C11b-type in order to simplify the consideration of an APB. The APB is characterized by a non-conservative anti-phase vector, *i.e.*, the composition is non-stoichiometric in the vicinity of the APB. A non-conservative APB typically originates from contact between two different particles nucleated out of phase away from each other, while a conservative APB can also be produced by slip deformation in a single particle [13,14]. Absence of an APB on the other θ’-θ interface located at the bottom of the twin boundary can be explained by assuming that both particles nucleated in phase, since the probability of in and out of phase nucleation is equivalent. Accordingly, these results suggest the following transformation process: First, two θ’ precipitates approach each other during the growth process. If the annealing temperature is relatively low a T-shaped junction is formed as observed for isothermal annealing at 723 K (Fig. 2(e)). On the other hand, if the annealing temperature is relatively high and enough to activate copper diffusion, the θ’ near the junction are disordered and/or resolved into the matrix, possibly to compensate increasing strain near the junction. Next, copper may be enriched into the junction to reduce strain near the junction and form a stable $\{013\}_{C11b}$ twin boundary. In this process, one of the θ’ precipitates is shortened to provide copper into the junction, resulting in the formation of a V-shaped junction rather than a T-shaped one. Since these procedures require active diffusion and thermal activation for nucleation, it is expected that these procedures are difficult to be activated at low temperature, and thus the V-shaped cluster can only be formed for the second aging at high temperature.

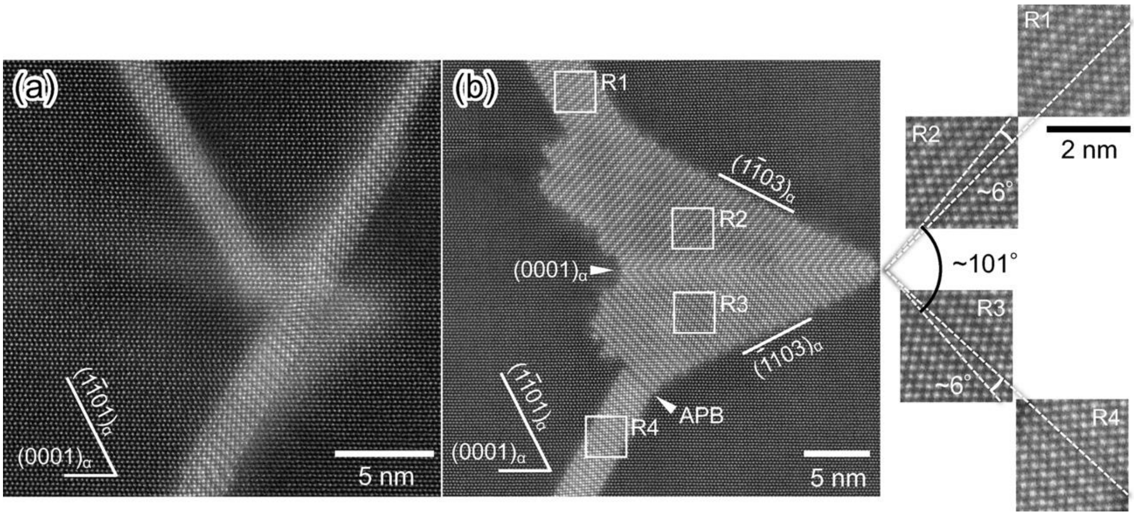

Fig. 9 (a) A HAADF-STEM image of a premature state of a cluster observed on the specimen after the second aging at 873 K for 1 h, where two θ' precipitates are about to be contact. (b) A HAADF-STEM image of the V-shaped cluster that is more developed than in (a).

Next, to understand the effect of transformation strain, we quantitatively evaluated lattice deformation from the HAADF-STEM image in Fig. 9(b). Firstly, lattice rotations of the θ' and the θ regions were simply measured on the image. The orientations of the lattice images were picked up from four regions denoted as R1, R2, R3, and R4 in Fig. 9(b). The angle between $(001)_{C11b}$ plane between R2 and R3 region was approximately 101° that is close to the ideal $\{013\}_{C11b}$ twin angle, estimated as 101.5° for lattice constants of a = 0.294 and c = 1.08 nm [15]. This verifies that the regions with $\{1\text{-}103\}_\alpha$ habit planes indeed correspond to the stable θ phase. In both sides of the θ' regions, R1 and R4, the lattices were rotated by approximately 6° with respect to R2 and R3 regions, respectively.

To evaluate distributions of lattice strain and rotation, the geometrical phase analysis (GPA) [16] was applied for the same image. In the GPA, two-dimensional strain and rotation are calculated with respect to a reference region based on local phase shift of the lattice fringes. In the present study, calculations were made for three regions; the α-titanium matrix, the upper part of the V-shaped cluster, and the lower part of the V-shaped cluster. The result for the matrix is shown in Fig. 10 and those for the V-shaped cluster are presented in Fig. 11. In Fig. 10, the x-direction is set along $[1\text{-}100]_\alpha$ and the reference region is defined as denoted in Fig. 10(a). Although the e_{xx} component of the strain (Fig. 10(a)) includes periodic noise due to probe scanning during image acquisition, it is found that any components of the elastic strains are small, whereas the upper part of the matrix is rotated against the lower part by approximately 2° (Fig. 10(d)). This suggests that twin formation of the θ phase introduces lattice rotation to the matrix, which may contribute to relaxation of transformation strain. In Fig. 11, the *x*-directions are respectively defined as parallel to $(001)_{C11b}$ plane for the upper and the lower parts of the V-shaped cluster and the reference regions are defined within the θ regions as denoted in Fig. 11(a). Similar to the measurement in Fig. 9(b), large rotations of more than 5° are found between the θ' and the θ regions on the both sides (Fig. 11(d)). In addition, a large negative e_{yy} component, reaching -0.05 or lower, is observed between the θ' and the θ regions, which represents the *c*-axis of the unit cell being shorter in the θ' phase than in the θ phase. In contrast, the e_{xx} component is not significantly different between the θ' and the θ phases, but gradually increases toward the habit planes. This may be related to the presence of step-like roughness near the $\{1\text{-}103\}_{\alpha}$ habit planes, which makes it difficult to compute the phase shift of the θ phase near the habit plane. Notably, rotation and strain are gradually changed from the θ to θ' regions on the upper part of the V-shaped cluster, but discontinuously changed on the lower part. In the latter case, the APB separates the θ' and the θ regions and plays a role of a buffer layer for compensating strain.

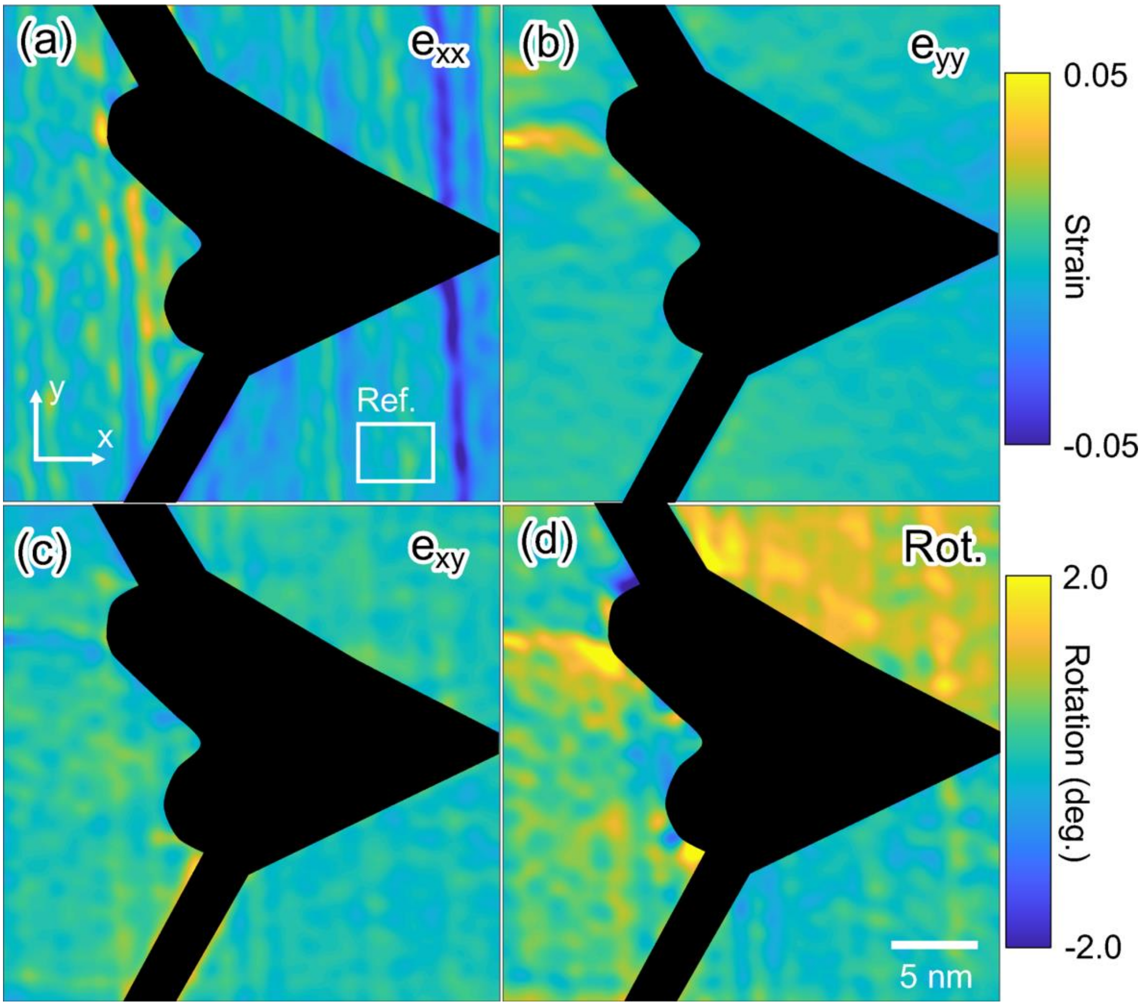

Fig. 10 (a)-(c) Strain and (d) rotation of the α-titanium matrix calculated on the HAADF-STEM image in Fig. 9(b) using the GPA method. The reference axes are shown in (a) and the reference state of the unit cell is defined by averaging over the white box in (a).

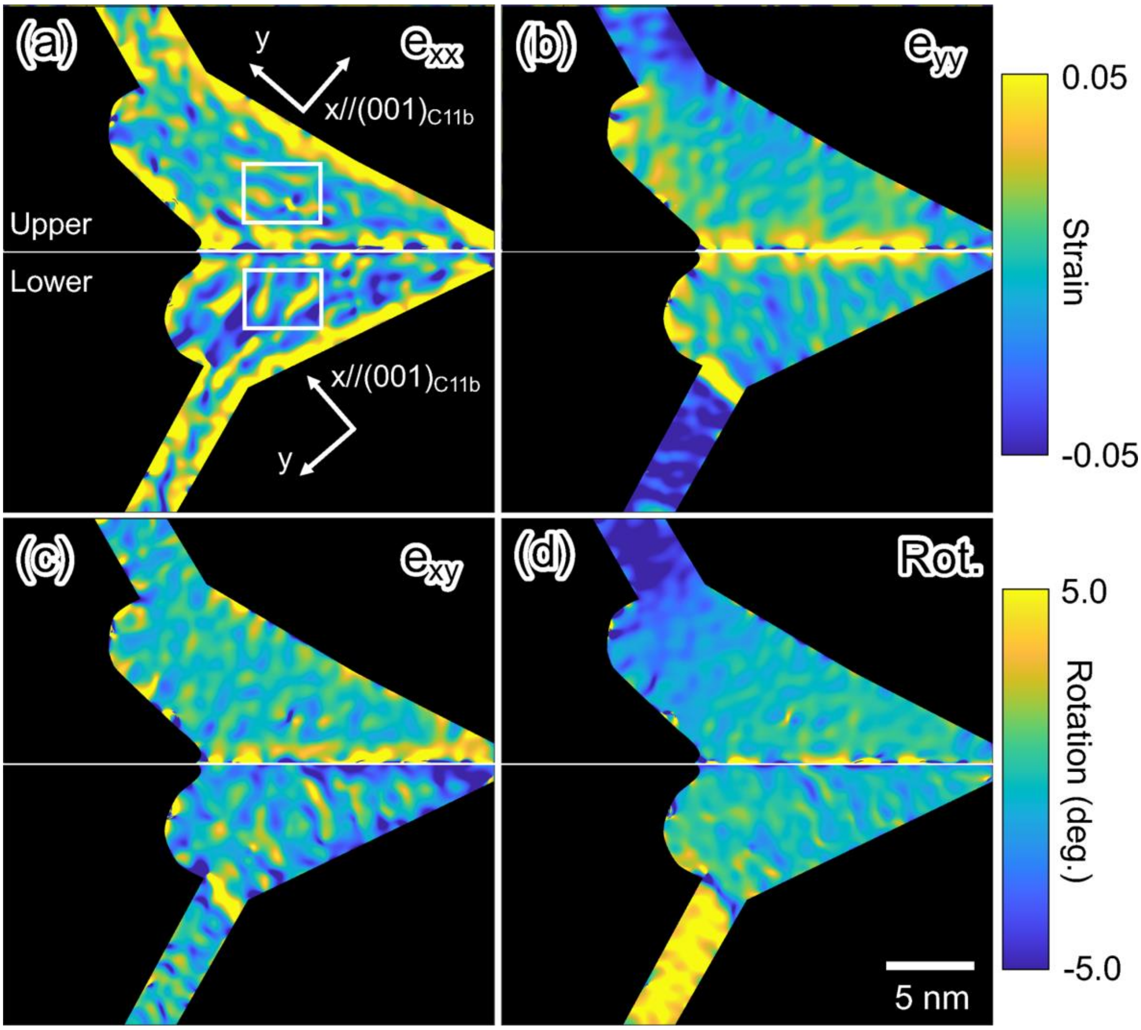

Fig. 11 (a)-(c) Strain and (d) rotation inside the precipitate calculated based on the HAADF-STEM image in Fig. 9(b) using the GPA method. The calculation was performed separately in the upper and lower parts of the precipitate. The reference axes in each calculation are described in (a), and the reference regions are shown by the white boxes in (a).

Consequently, the results of the strain analysis suggest that the θ' and the θ phases are mainly characterized by a lattice contraction along *c*-axis of the C11b-type structure reaching nearly 5 percent of the θ unit cell, *i.e.* ~0.05 nm, and a lattice rotation of approximately 6°. The rotation of approximately 2° is also observed for the nearby matrix, both of which can be related to the relaxation of transformation strain. Since inhomogeneous elastic strain field functions as resistance for dislocation motion, it is expected that the relaxation of strain by the formation of θ phases give an additional impact on the hardness, which possibly explains the drastic softening during the two-step aging.

5. Conclusion

In this study, precipitation behavior in Ti-2.3 wt.%Cu alloy was investigated by using SEM and (S)TEM. The following results were obtained.

(1) In the isothermal aging, the θ’ and the θ precipitates are nucleated independently in the matrix. The phase fractions of the θ’ and the θ phases depend on the aging temperature and aging time. In particular, only the θ’ precipitates are observed with low aging temperature of 673 K. Based on a series of (S)TEM and SEM observations, a schematic TTP diagram is constructed as shown in Fig. 5.

(2) In the two-step aging, where temperature is switched from the single phase region of θ’ phase (673 K) to the two phase region of θ’ and θ phases (873 K), multiple θ’ precipitates form the characteristic V-shaped clusters. In such clusters, the θ phase is nucleated with a stable $\{013\}_{C11b}$ twin boundary, driven by active copper diffusion in the matrix. The presence of the θ phase can be evidenced by a transition of the habit planes near the junction, changing from $\{1\text{-}101\}_{\alpha}$ to $\{1\text{-}103\}_{\alpha}$, the latter of which corresponds to the θ phase. In the later stage, the clusters are totally transformed into the θ phase.

(3) The hardness decreases drastically in the second aging in the two-step aging. This drastic drop of the hardness can be explained by coarsening of the precipitates, decrease in the number density, and the relaxation of the strain field accompanied by the θ’-θ transformation.

Acknowledgements

This study was supported by Japan Society for the Promotion of Science (JSPS) KAKENHI Grant Number JP18K0134.

References

[1] S. Banerjee, and P. Mukhopadhyay: *Phase Transformations: Examples from Titanium and Zirconium Alloys*, 1st ed., Elsevier Science, Oxford, 2010.

[2] C. Leyens, M. Peters: *Titanium and Titanium Alloys: Fundamentals and Applications*, Wiley-VCH Verlag GmbH & Co. KGaA, Weinheim, 2003.

[3] D. J. Truax, and C. J. McMahon, Jr.: *Mater. Sci. Eng.*, 1974, vol. 13, pp. 125-139.

[4] P. Kwasniak, H. Garbacz, and K. J. Kurzydlowski: *Acta Mater.*, 2016, vol. 102, pp. 304-314.

[5] H. Otsuka, H. Fujii, K. Takahashi, and K. Mori: *Nippon Steel Technical Report*, 2013, vol. 396,

pp. 56-62.
[6] H. Okamoto: *Phase Diagram for Binary Alloys*, 2nd ed., ASM International, Materials Park, 2010.
[7] M. Mitsuhara, T. Masuda, M. Nishida, T. Kunieda, and H. Fujii: *Metall. Mater. Trans. A*, 2016, vol. 47A, pp. 1544-1553.
[8] A. Biswas, D. J. Siegel, C. Wolverton, and D. N. Seidman: *Acta Mater.*, 2011, vol. 59, pp. 6187-6204.
[9] J. C. Williams, R. Taggart, and D. H. Polonis: *Metall. Trans.*, 1971, vol. 2, pp. 1139-1148.
[10] O. Taguchi, and Y. Iijima: *Phios. Mag. A*, 1995, vol. 72, pp. 1649-1655.
[11] H. Mehrer: *Diffusion in solids*, Springer-Verlag Berlin Heidelberg, Berliin, 2007.
[12] E. Virtanen, C. J. Van Tyne, B. S. Levy, and G. Brada: J. Mater. Processing Technology., 2013, vol. 213, pp. 1364-1369.
[13] M. J. Marcinkowski: *Theory and direct observation of antiphase boundaries and dislocations in superlattices, in: Electron Microscopy and Strength of Crystals; Proceedings of the First Berkeley International Materials Conference (Ed. By G. Thomas and J. Washbuurn)*, Interscience Publishers, New York, 1963, pp. 333-440.
[14] Y. -Q. Sun: *Intermetallic Compounds: Principles and Practice, Vol. 1 (Ed. By J. H. Westbrook and R. L. Fleischher)*, John Wiley & Sons Ltd., New York, 1998, pp. 495-518.
[15] V. N. Chebotnikov, and V. V. Molokanov: *Inorg. Mater.*, 1990, vol. 26, pp. 808-811.
[16] M. J. Hytch, E. Snoeck, R. Kilaas: *Ultramicroscopy*, 1998, vol. 74, pp. 131-146.

Tables:

Table 1. Chemical composition (wt. %) of the alloy used in the present study.

C	Ni	Cr	Cu	Fe	H	O	N	Ti
0.003	0.011	0.001	2.26	0.020	0.001	0.034	0.005	Bal.

Table 2 Tempering parameters, *P*, calculated for aging at 723 K and 873 K.

Temperature (K)	Aging time (h)	Tempering parameters
723	1	14,460
723	10	15,183
723	100	15,906
723	1000	16,629

873	1	17,460
873	10	18,333
873	100	19,206

Figure Captions:

Fig. 1 Age-hardening curves under different aging temperatures. The curves for 673, 773, and 873 K are reproduced from Ref. [7].

Fig. 2 (a)-(c) Crystal orientation maps for the specimen aged at 723 K for 100, 600, 1000 h, respectively. (d)-(f) SEM images obtained from the boxes in (a)-(c), respectively, and (g)-(i) corresponding trace lines calculated from the measured crystal orientations.

Fig. 3 Length histograms of θ’ (orange) and θ (blue) precipitates for the specimen aged at 723 K for (a) 100 h, (b) 600 h, and (c) 1000 h, respectively. Frequency is normalized such that integration over two histograms (θ’+θ) yields unity.

Fig. 4 Time-Temperature-Precipitate diagram for the Ti-2.3 wt.% Cu alloy constructed based on STEM and SEM observations. Open square indicates two phase regions of θ‘ and θ, filled circles single phase region of θ’, and cross marks means that no precipitates were observed.

Fig. 5 Age-hardening curves for the two-step aging from 673 K for 100 h to 873 K for 100 h. For comparison, single-step aging curves for 673, 723, 773, and 873 K for this time-spun are plotted again.

Fig. 6 STEM-HAADF images for the specimens (a), (b) aged at 673 K for 100 h and (c), (d) after the second aging at 873 K for 1 h.

Fig. 7 STEM-HAADF images for the specimens after the second aging at 873 K for (a), (b) 10 h, and (c), (d) 100 h.

Fig. 8 (a) Development of fraction of θ phase in the regions occupied by precipitates during the second aging at 873 K. For the clustered precipitates including both phases, length of θ phase was measured as partial length of $\{1\text{-}103\}_{\alpha}$ habit planes denoted as b in the inset illustration in (a). (b) Development of the number density of the precipitates, in which clustered precipitates were counted as a single precipitate.

Fig. 9 (a) A HAADF-STEM image of a premature state of a cluster observed on the specimen after the second aging at 873 K for 1 h, where two θ’ precipitates are about to be contact. (b) A HAADF-STEM image of the V-shaped cluster that is more developed than in (a).

Fig. 10 (a)-(c) Strain and (d) rotation of the α-titanium matrix calculated on the HAADF-STEM image in Fig. 9(b) using the GPA method. The reference axes are shown in (a) and the reference state of the unit cell is defined by averaging over the white box in (a).

Fig. 11 (a)-(c) Strain and (d) rotation inside the precipitate calculated based on the HAADF-STEM image in Fig. 9(b) using the GPA method. The calculation was performed separately in the upper and lower parts of the precipitate. The reference axes in each calculation are described in (a), and the reference regions are shown by the white boxes in (a).

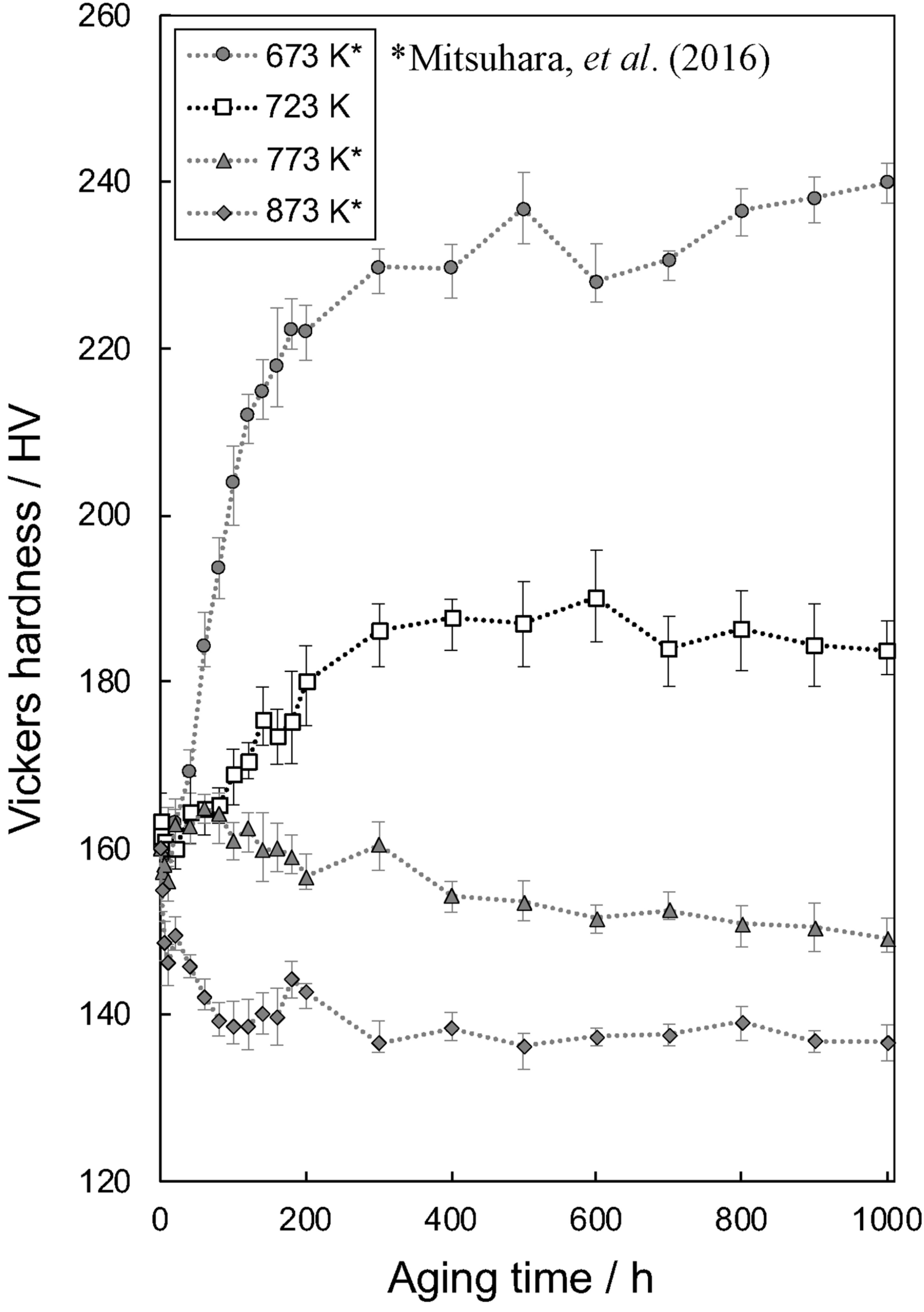

673 K*
723 K
773 K*
873 K*
*Mitsuhara, et al. (2016)
Vickers hardness / HV
Aging time / h
260
240
220
200
180
160
140
120
0
200
400
600
800
1000

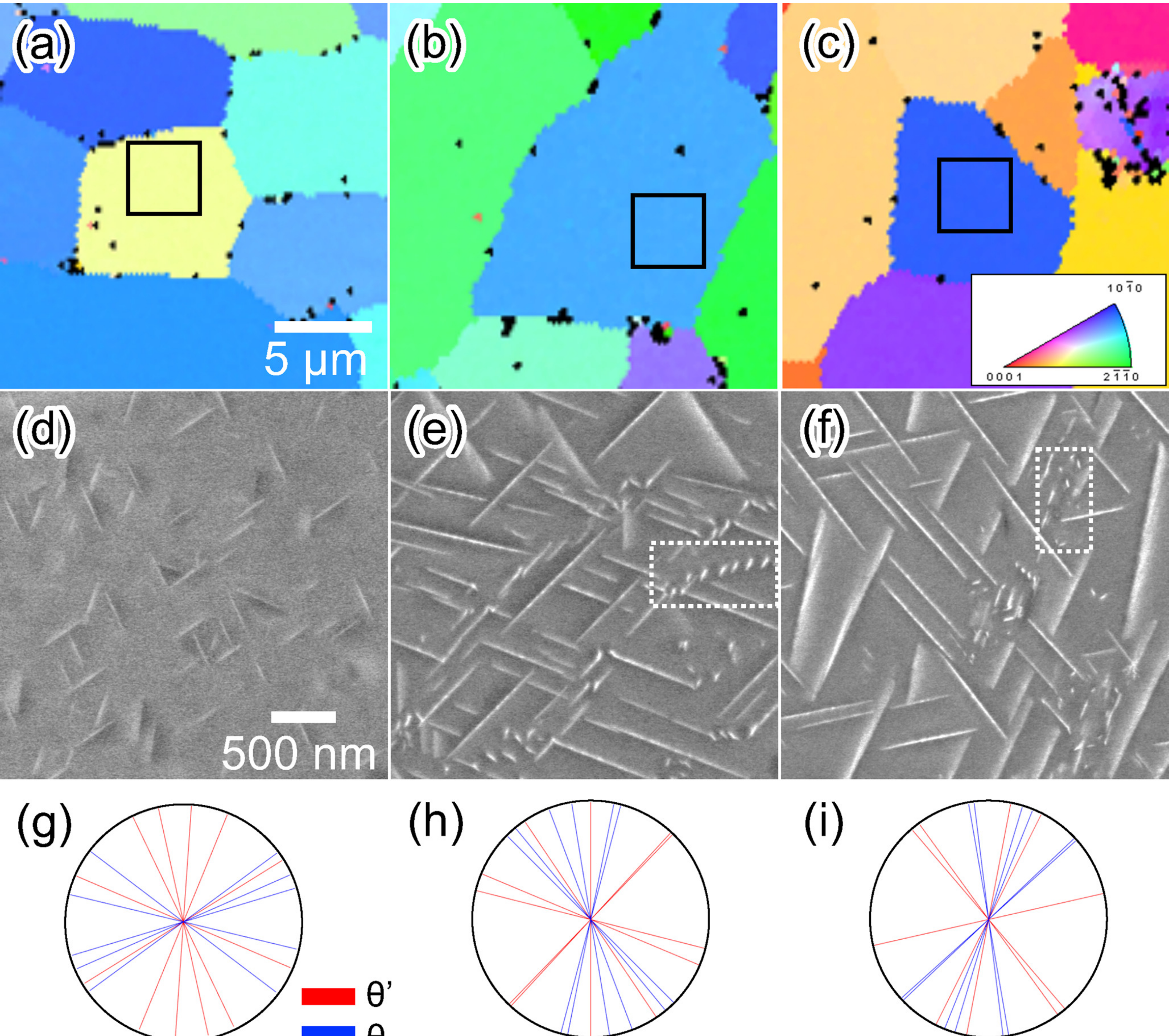

(a)
(b)
(c)
5 µm
$10\bar{1}0$
0001
$2\bar{1}\bar{1}0$
(d)
(e)
(f)
500 nm
(g)
(h)
(i)
θ'
θ

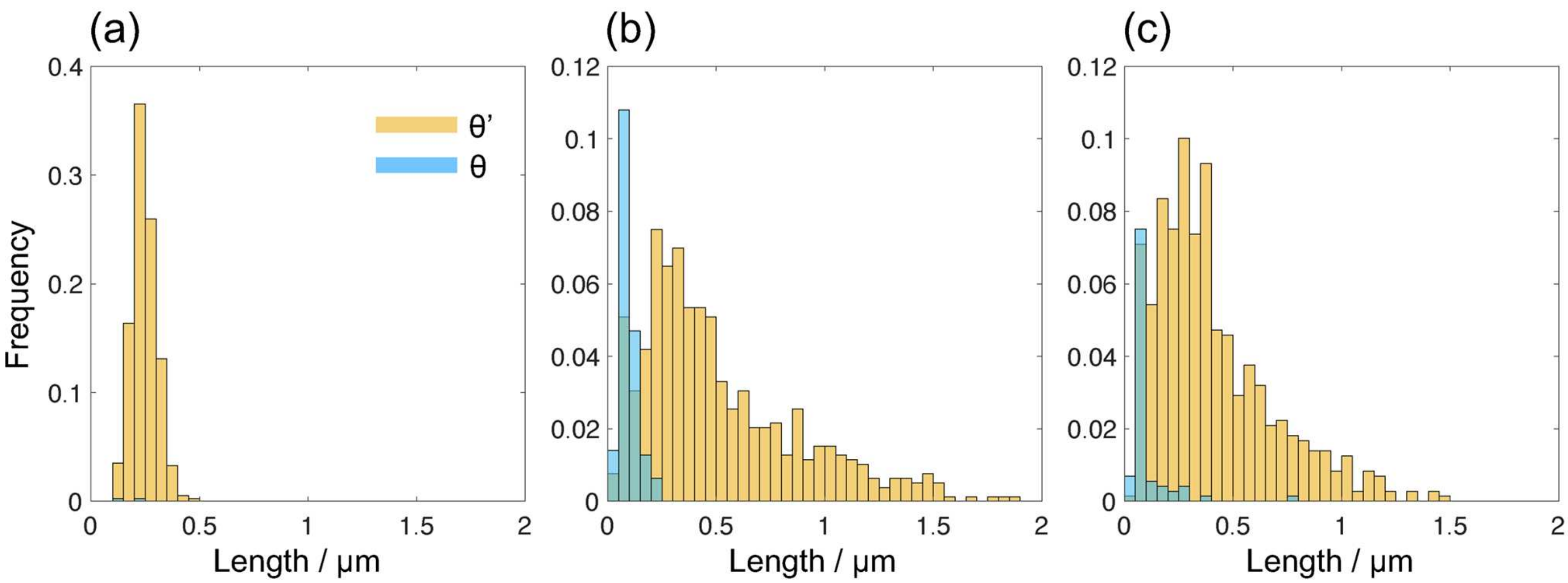
(a)
(b)
(c)
θ'
θ
Frequency
Length / μm
Length / μm
Length / μm

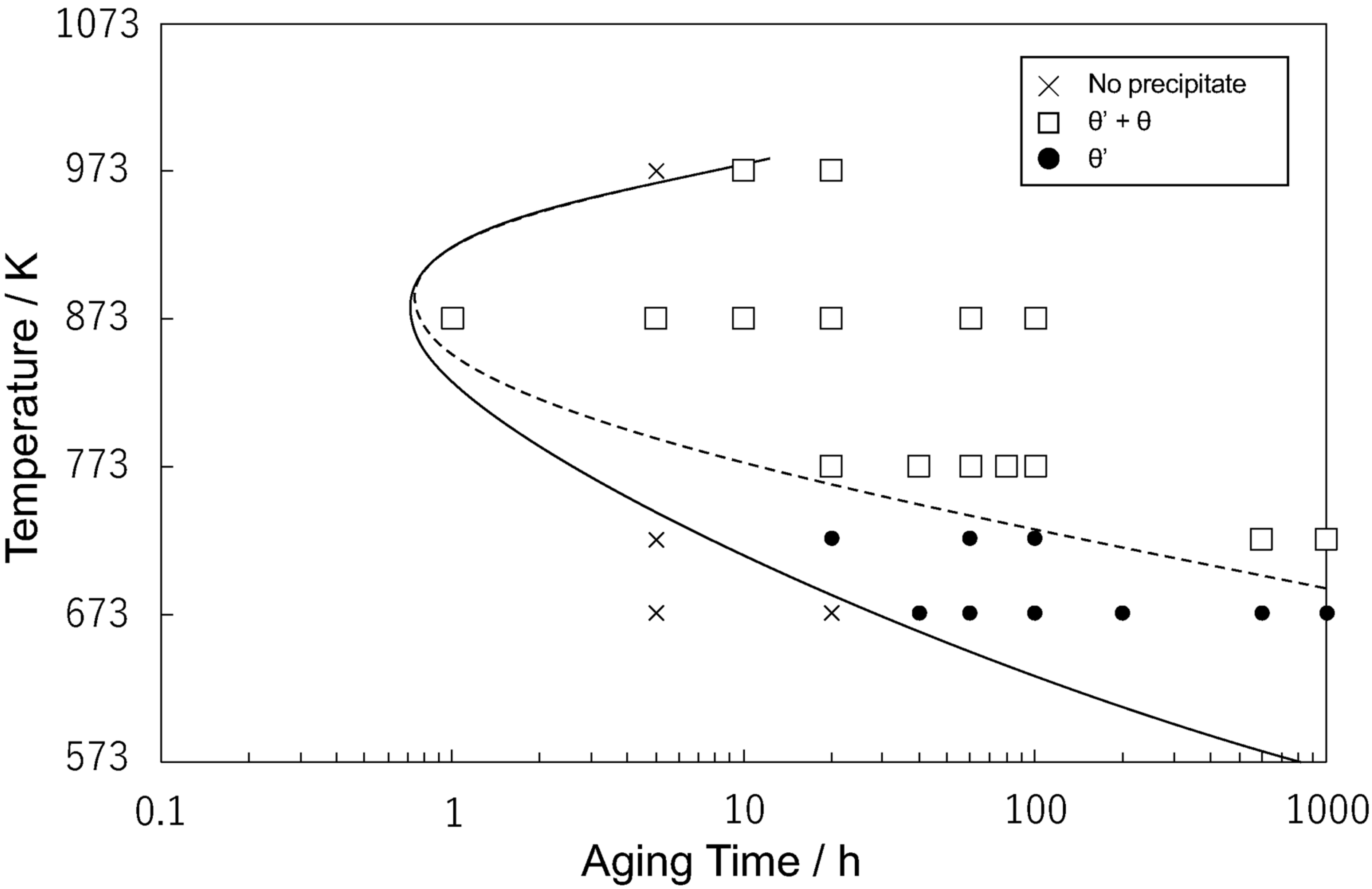

1073
973
873
773
673
573
Temperature / K
0.1
1
10
100
1000
Aging Time / h
No precipitate
θ' + θ
θ'

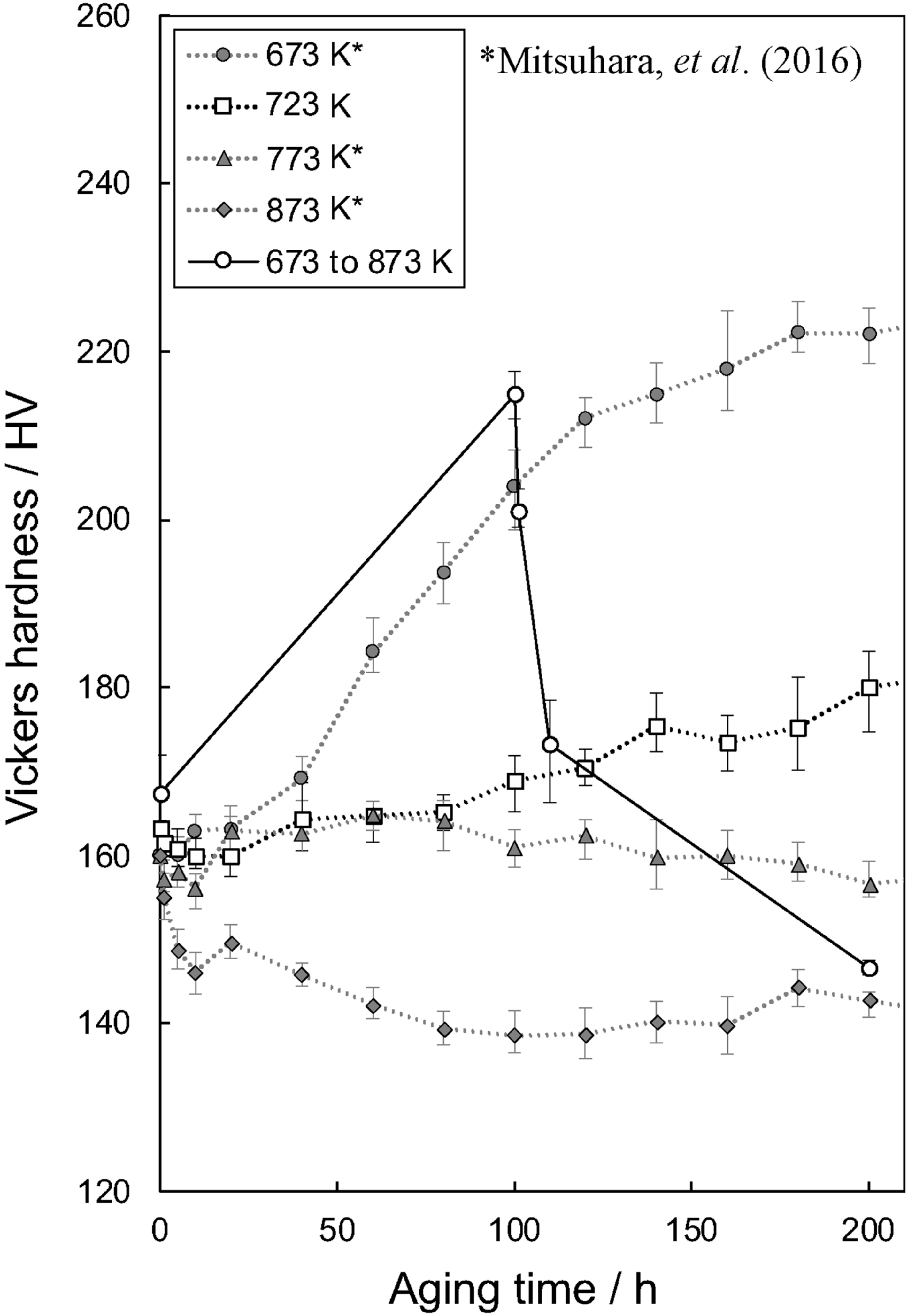

673 K*
723 K
773 K*
873 K*
673 to 873 K
*Mitsuhara, et al. (2016)
Vickers hardness / HV
Aging time / h
260
240
220
200
180
160
140
120
0
50
100
150
200

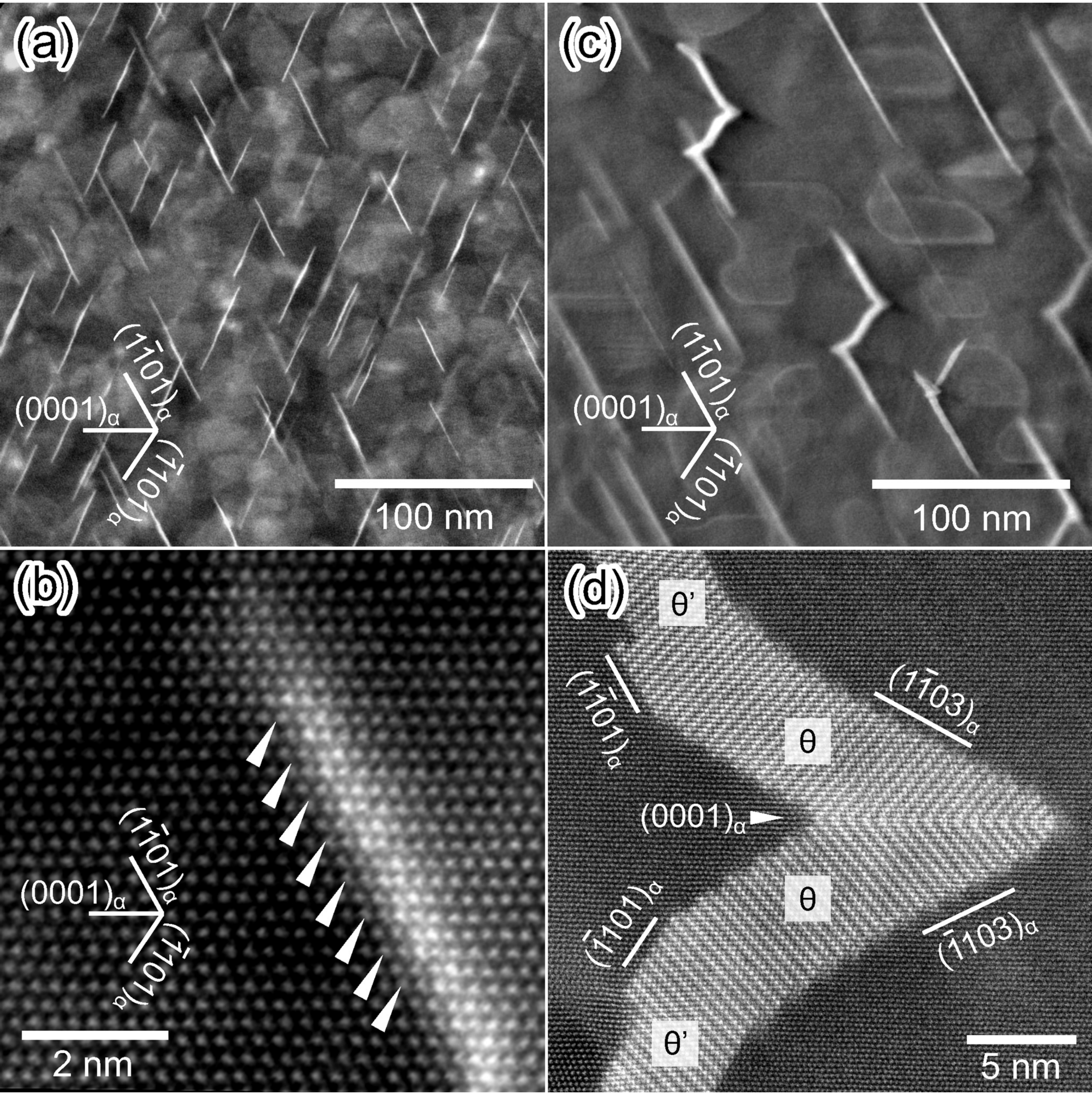

(a)
$(\bar{1}\bar{1}01)_\alpha$
$(0001)_\alpha$
$(\bar{1}101)_\alpha$
100 nm
(b)
$(\bar{1}\bar{1}01)_\alpha$
$(0001)_\alpha$
$(\bar{1}101)_\alpha$
2 nm
(c)
$(\bar{1}\bar{1}01)_\alpha$
$(0001)_\alpha$
$(\bar{1}101)_\alpha$
100 nm
(d)
θ'
$(\bar{1}\bar{1}01)_\alpha$
$(1\bar{1}03)_\alpha$
θ
$(0001)_\alpha$
θ
$(\bar{1}101)_\alpha$
$(\bar{1}103)_\alpha$
θ'
5 nm

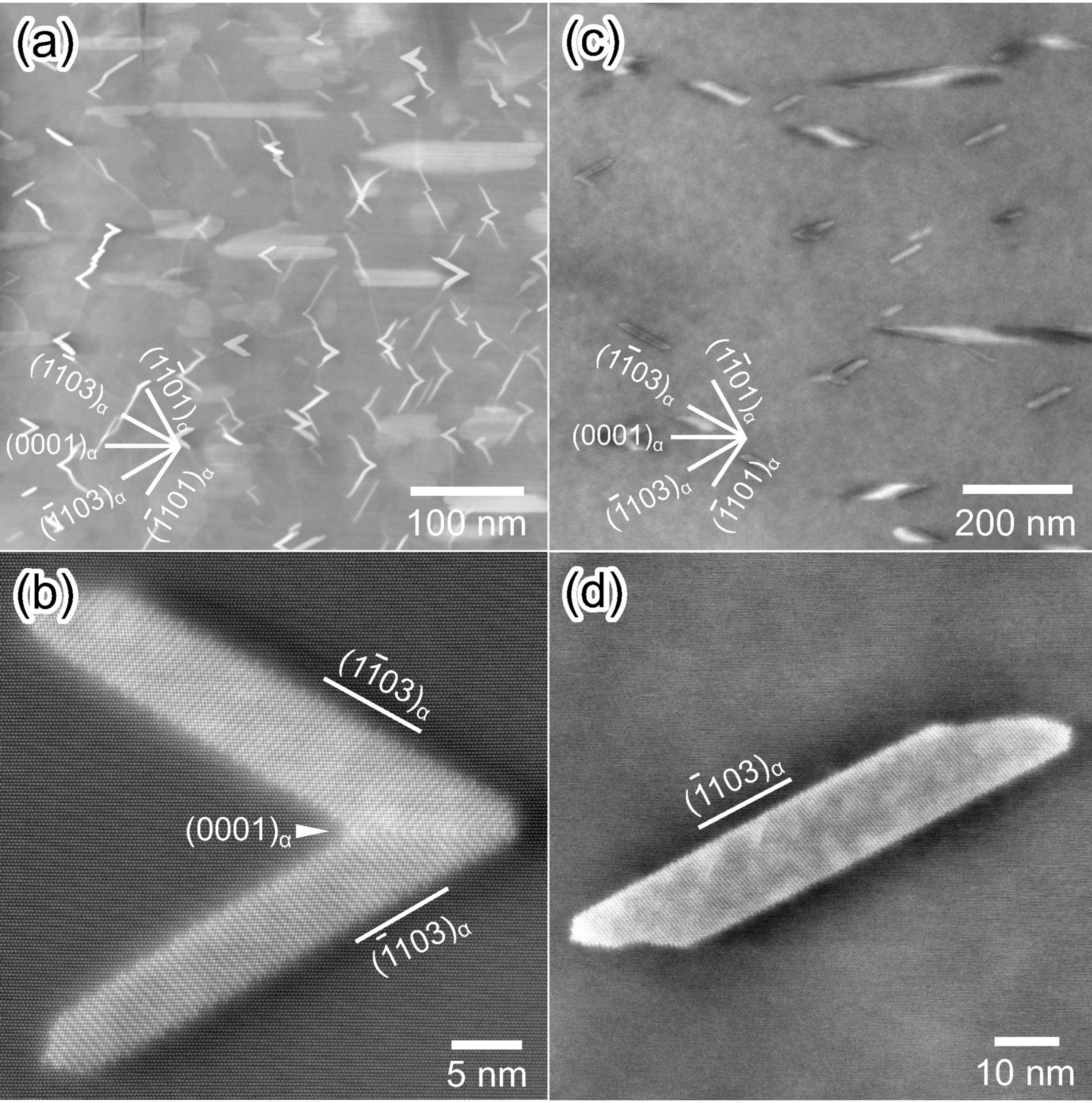

(a)
$(1\bar{1}03)_\alpha$
$(1\bar{1}01)_\alpha$
$(0001)_\alpha$
$(\bar{1}103)_\alpha$
$(\bar{1}101)_\alpha$
100 nm
(c)
$(1\bar{1}03)_\alpha$
$(1\bar{1}01)_\alpha$
$(0001)_\alpha$
$(\bar{1}103)_\alpha$
$(\bar{1}101)_\alpha$
200 nm
(b)
$(1\bar{1}03)_\alpha$
$(0001)_\alpha$
$(\bar{1}103)_\alpha$
5 nm
(d)
$(\bar{1}103)_\alpha$
10 nm

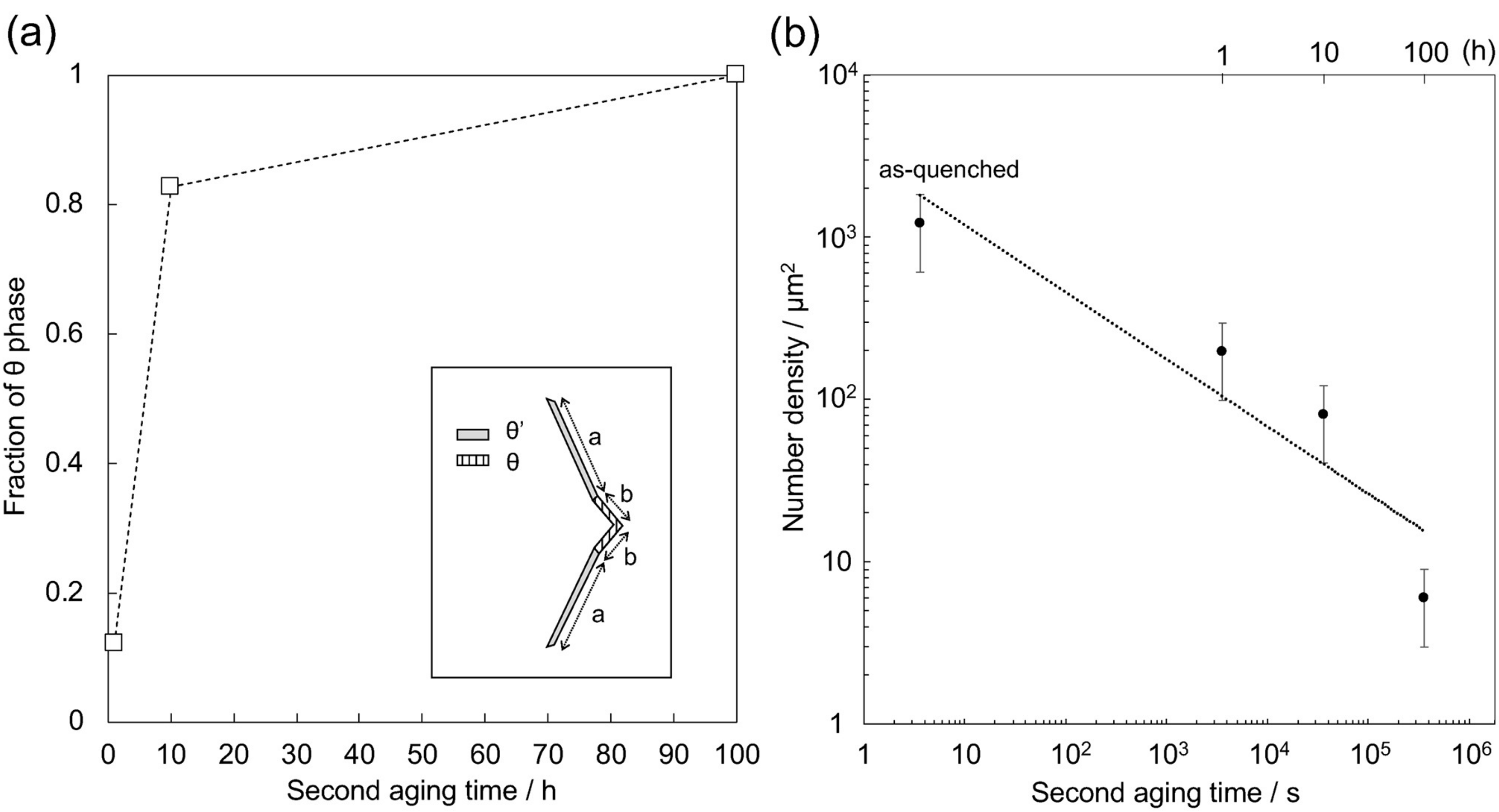

(a)
Fraction of θ phase
Second aging time / h
θ'
θ
a
b
b
a
(b)
as-quenched
Number density / μm2
Second aging time / s
(h)

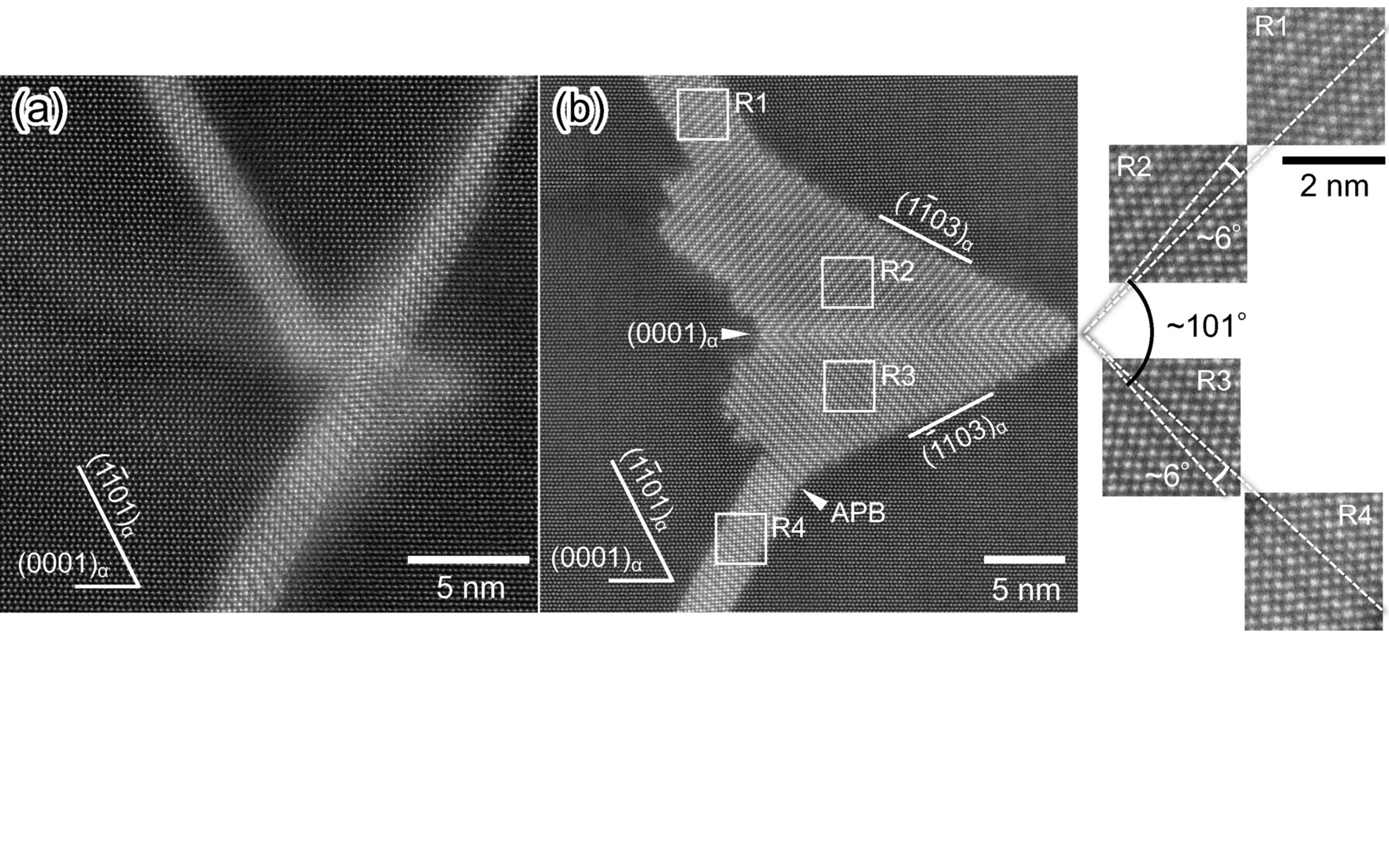

(a)
$(\bar{1}\bar{1}01)_\alpha$
$(0001)_\alpha$
5 nm
(b)
R1
$(1\bar{1}03)_\alpha$
R2
$(0001)_\alpha$
R3
$(\bar{1}103)_\alpha$
$(\bar{1}\bar{1}01)_\alpha$
APB
R4
$(0001)_\alpha$
5 nm
R1
R2
2 nm
~6°
~101°
R3
~6°
R4

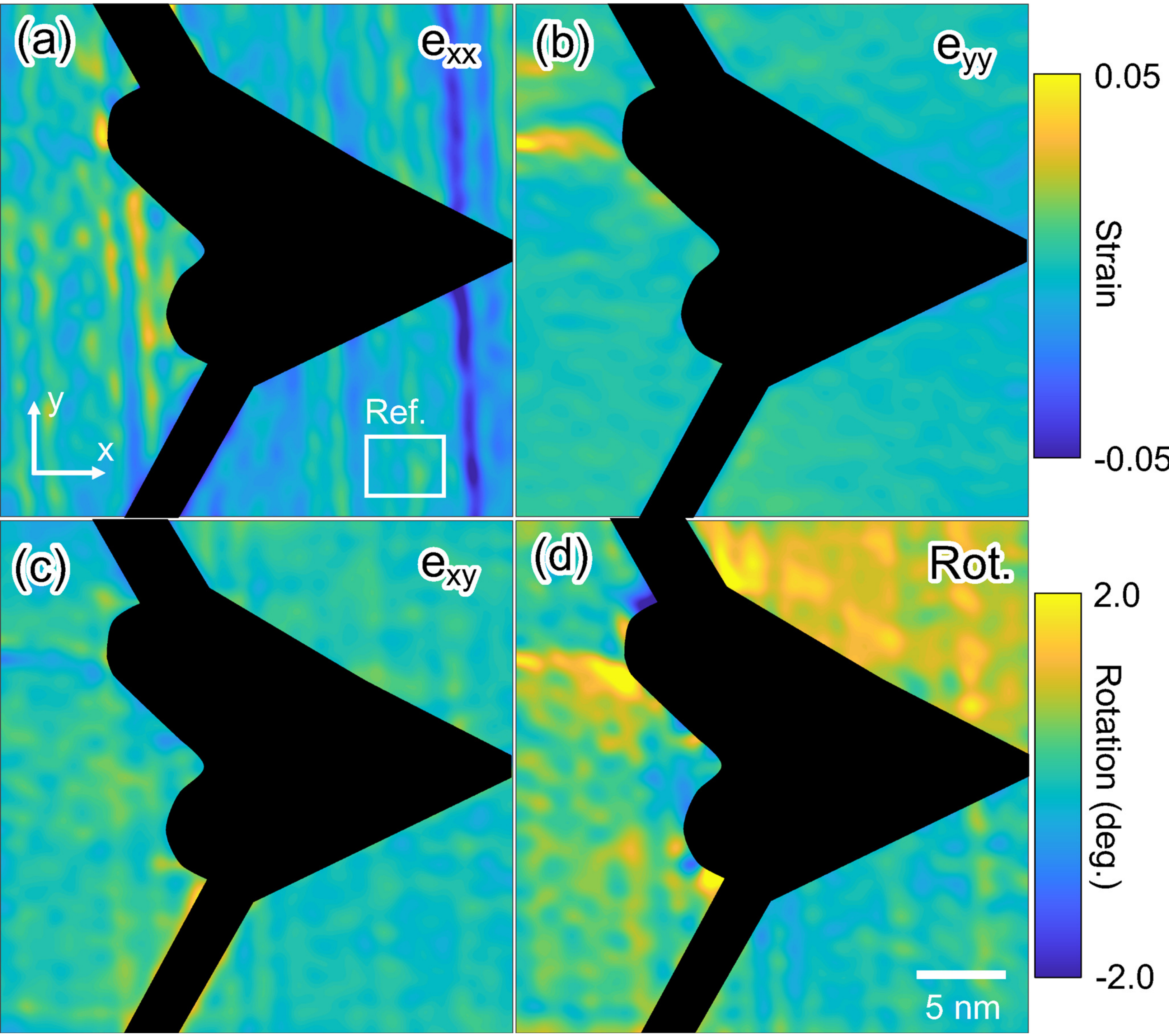

(a)
e_{xx}
y
x
Ref.
(b)
e_{yy}
0.05
Strain
-0.05
(c)
e_{xy}
(d)
Rot.
2.0
Rotation (deg.)
-2.0
5 nm

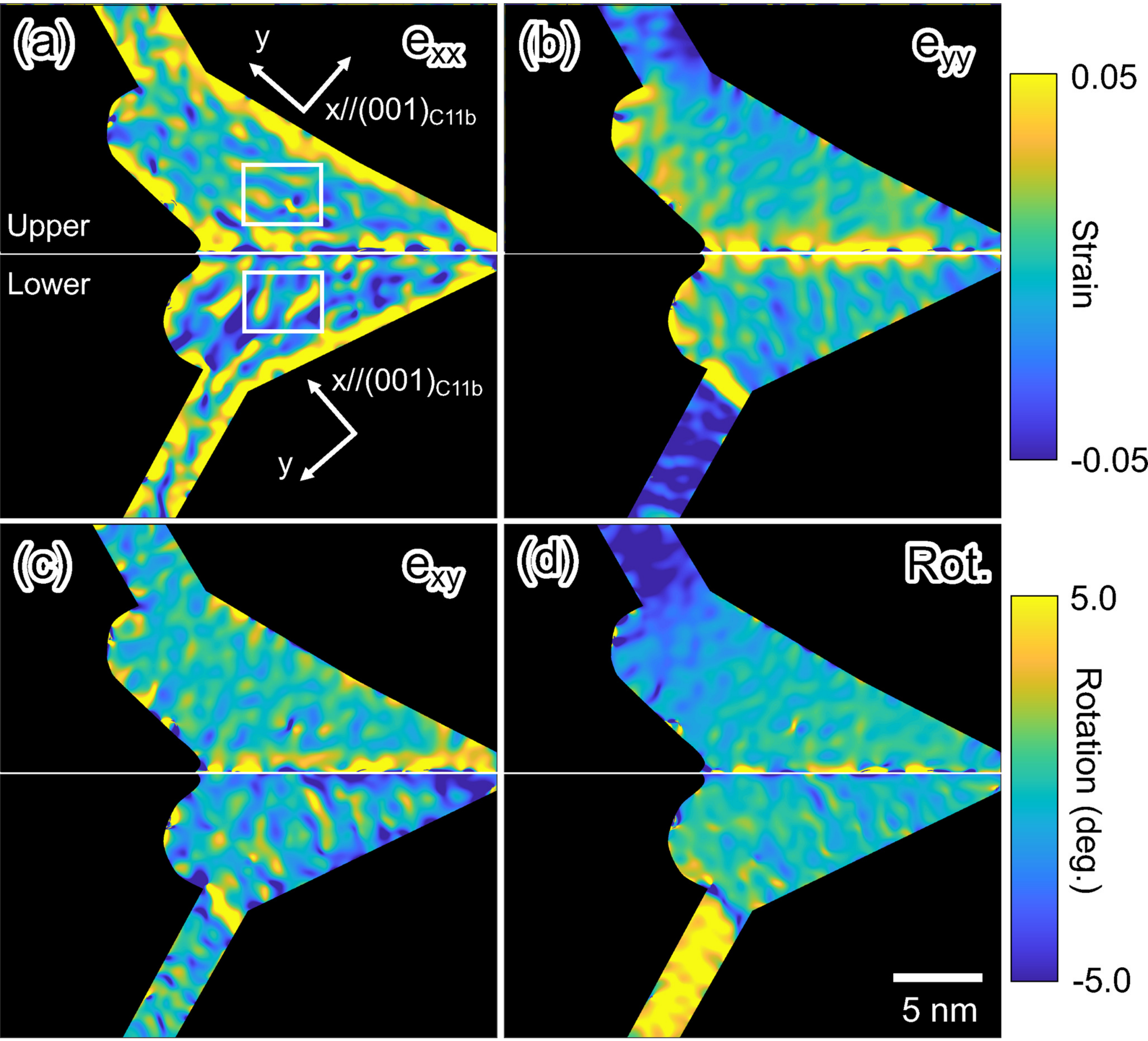

(a)
e_{xx}
y
x//(001)$_{C11b}$
Upper
Lower
x//(001)$_{C11b}$
y
(b)
e_{yy}
0.05
Strain
-0.05
(c)
e_{xy}
(d)
Rot.
5.0
Rotation (deg.)
-5.0
5 nm